



## Simulation of brittle and ductile fracture in an impact loaded prenotched plate

R.C. BATRA and M.H. LEAR

*Department of Engineering Science and Mechanics, MC 0219, Virginia Polytechnic Institute and State University, Blacksburg, VA 24061, U.S.A.*

Received 26 January 2003; accepted in revised form 10 February 2004

**Abstract.** We analyze the initiation and propagation of a crack from a point on the surface of a circular notch-tip in an impact loaded prenotched plate. The material of the plate is assumed to exhibit strain hardening, strain-rate hardening, and softening due to the rise in temperature and porosity. The degradation of material parameters due to the evolution of damage in the form of porosity is considered. Brittle failure is assumed to initiate when the maximum tensile principal stress at a point reaches a critical level. Ductile failure is assumed to ensue when the effective plastic strain reaches a critical value. A crack initiating from the node where a failure first occurs is taken to propagate to the adjacent node that has the highest value of the failure parameter (the maximum tensile principal stress or the effective plastic strain). The opening and propagation of a crack are modeled by the node release technique. Surface tractions and the normal component of the heat flux are taken to be null on the newly created crack surfaces. For the brittle failure, the stress field around the crack tip resembles that in mode-I deformations of a prenotched plate loaded in tension. The distribution of the effective plastic strain in a small region around the surface of the notch-tip is not affected much by the initiation of a ductile fracture there except for a shift in the location of the point where the effective plastic strain is maximum. The initiation of the ductile failure is delayed when a crack is opened at the point where the brittle failure ensues.

**Key words:** Crack propagation, failure mode transition, finite element solution, hyperbolic heat equation, micro-porous thermoviscoplastic material.

### 1. Introduction

Modeling the propagation of a crack during the solution of a transient mechanical problem by the finite element method (FEM) is challenging since the mesh needs to be modified and boundary conditions of null tractions imposed on the newly created crack surfaces. Three strategies used to study fracture are: (i) reducing stresses in the failed region through the evolution of damage in the material, (ii) representing a crack as two traction free surfaces, and (iii) introducing cohesive elements along interelement boundaries that are weak in shear and tension but very strong in compression (Needleman, 1987). Whereas every component of the stress tensor is assumed to drop either gradually or instantaneously to zero in the first approach, only tractions normal and tangent to the crack surfaces drop suddenly to zero in the second approach. It is easier to model crack propagation along inter-element boundaries than to model intra-element crack propagation since in the former no new elements are created while in the latter they are. However, requiring a crack to propagate along an inter-element boundary necessitates an *a priori* assumption on the path of the propagating crack that may not correctly represent the crack's true path. The accuracy of the inter-element approach can be improved by using a very fine mesh in the region where cracks are expected to initiate and propagate.

Here crack propagation along inter-element boundaries is used to analyze the initiation and propagation of brittle and ductile fractures from points in the vicinity of a notch-tip in an impact loaded prenotched metallic plate. Previous numerical studies (e.g., see, Needleman and Tvergaard, 1995; Zhou et al. 1996b; Batra and Nechitailo, 1997; Batra and Gummalla, 2000; Batra and Ravisankar, 2000; Batra and Jaber, 2001; Batra et al., 2003), of this problem have focused on the initiation of the two failure modes and the impact speed at which the failure mode transitions from brittle to ductile. The interest in the problem was generated by the experimental work of Kalthoff and Winkler (1987) and Kalthoff (1987) who observed that the failure mode in an impact loaded prenotched steel plate transitioned from brittle to ductile with an increase in the impact speed. Whereas Batra and Ravisankar (2000) studied 3-dimensional locally adiabatic deformations of the thermoviscoplastic impactor and the thermoviscoplastic plate, other works analyzed plane strain deformations of the system. Except for Batra and Nechitailo (1997), Batra and Ravisankar (2000) and Batra and Gummalla (2000), other works replaced the action of the impactor on the plate by prescribing a normal velocity on the impacted surface of the plate. The 3-dimensional simulations of Batra and Ravisankar (2000) have shown that deformations of the central 3/4th of the plate closely resemble those obtained from the assumption of plane strain but those of points on or adjacent to the front and the rear surfaces of the plate are quite different. Batra and Gummalla (2000) have delineated the effect of different material and geometric parameters on the initiation of the two failure modes. Batra and Jaber (2001) found that four thermoviscoplastic relations calibrated against the same torsion test data predicted quite different values of the impact speed at which failure mode transitions from brittle to ductile. However, deformations of points around the notch-tip were qualitatively similar for the four thermoviscoplastic relations; a similar result was obtained by Batra and Kim (1990) and Batra and Chen (2002) for simple shearing deformations of a thermoviscoplastic body. Batra et al. (2003) found that the shape of the notch-tip and the presence of a circular hole ahead of the notch-tip significantly affected when and where failure initiated, and hence the failure mode transition speed. For example, for a sharp elliptic notch, the ductile failure preceded the brittle failure at all impact speeds but for a circular notch-tip the failure mode transitioned from brittle to ductile with an increase in the impact speed. It should be mentioned that in Zhou et al.'s (1996a) experiments on prenotched steel plates only ductile failure was observed. They found that no failure ensued at low impact speeds but at high impact speeds a shear band initiating from a point on the notch-tip propagated nearly parallel to the notch-axis, got arrested and a crack originated from the shear band tip. They attributed the difference in their and Kalthoff's experimental results to different values of material parameters. Kalthoff listed only the Rockwell hardness for the steel tested and did not provide stress-strain curves. Zhou et al. (1996b) evaluated material parameters for their steel by curve fitting. Ravi-Chandar et al. (2000) examined experimentally failure modes in asymmetrically loaded prenotched plates made of two polymers, polycarbonate (PC) and polymethylmethacrylate (PMMA); the experimental set up is similar to that of Kalthoff. With an increase in the impact speed, PC was shown to exhibit a failure mode transition from ductile to brittle at about 29 m/s, and a second failure mode transition from brittle to ductile as the impact speed was increased beyond 55 m/s. The second transition resulted in a shear band near the crack tip. No failure mode transition occurred in PMMA because of its inability to undergo large inelastic deformations under tension.

Whereas the failure mode transition in the Kalthoff problem has been analyzed numerically as noted above, how the crack opening at the point of initiation of brittle failure influences

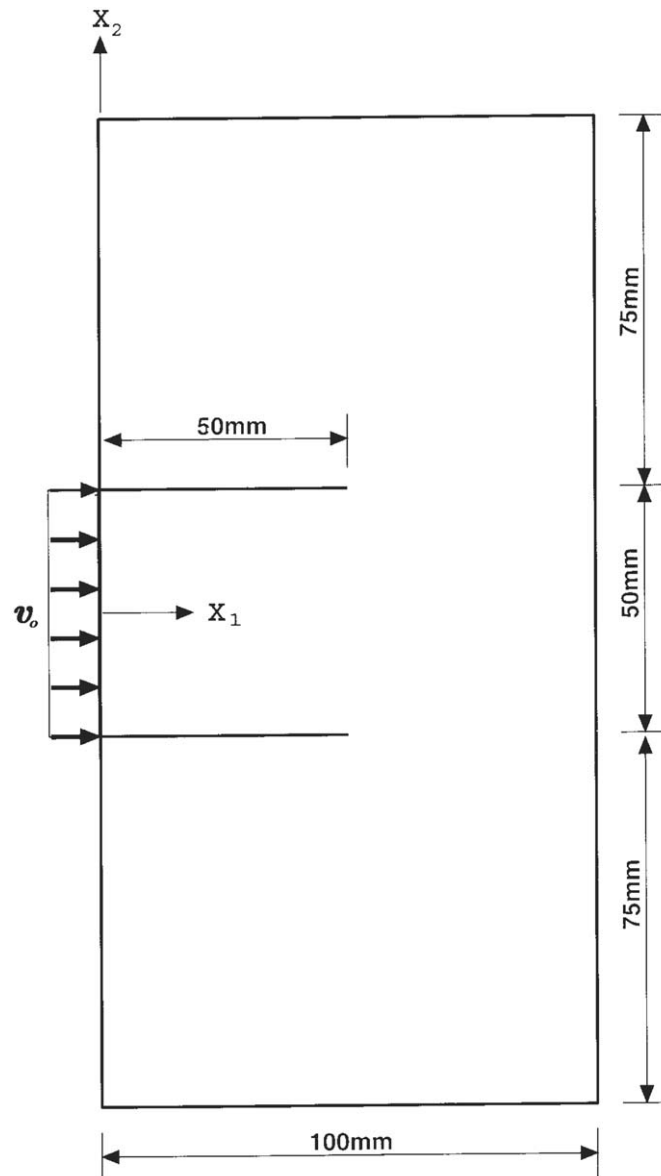


Figure 1. Schematic sketch of the problem studied. The notch-tip radius is 0.15 mm.

deformation fields around the notch-tip and the initiation time of ductile failure has not been scrutinized yet; we do so here.

## 2. Formulation of the Problem

A schematic sketch of the problem studied is shown in Figure 1. The left edge surface of the prenotched steel plate with two edge notches is struck, at normal incidence, by a cylindrical rod of diameter equal to the distance between the two notches. The impactor and the plate are made of the same material that is modeled as isotropic, homogeneous, microporous and thermoviscoplastic. We use rectangular Cartesian coordinates and the referential description

of motion to describe their deformations which are governed by the balance of mass, the balance of linear momentum, the balance of moment of momentum, and the balance of internal energy. Equations expressing these balance laws are:

$$[\rho(1-f)J]^{\bullet} = 0, \quad (1)$$

$$\rho_0(1-f_0)\dot{v}_i = T_{i\alpha,\alpha}, \quad i, j = 1, 2, \alpha = 1, 2, \quad (2)$$

$$T_{i\alpha}F_{j\alpha} = T_{j\alpha}F_{i\alpha}, \quad (3)$$

$$\rho_0(1-f_0)\dot{e} = -Q_{\alpha,\alpha} + T_{i\alpha}\dot{F}_{i\alpha}. \quad (4)$$

Here  $\rho$  is the present mass density,  $f$  the porosity (i.e., the volume fraction of voids),  $J = \det \mathbf{F}$ ,  $F_{i\alpha} = x_{i,\alpha} = \partial x_i / \partial X_\alpha$  the deformation gradient,  $\mathbf{x}$  the present position at time  $t$  of a material particle located at the place  $\mathbf{X}$  in the reference configuration,  $\mathbf{T}$  the first Piola-Kirchhoff stress tensor,  $e$  the specific internal energy,  $\mathbf{Q}$  the present heat flux measured per unit reference area,  $\mathbf{v}$  the velocity of a material particle, a superimposed dot indicates the material time derivative, and a repeated index implies summation over the range of the index. Greek indices refer to coordinates in the reference configuration, and Latin indices to coordinates in the present configuration.

We assume that the strain-rate tensor  $\mathbf{D}$  defined by  $D_{ij} = (v_{i,j} + v_{j,i})/2$ ,  $v_{i,j} = \partial v_i / \partial x_j$ , has the additive decomposition into an elastic part  $\mathbf{D}^e$  and a plastic part  $\mathbf{D}^p$ , viz.,

$$\mathbf{D} = \mathbf{D}^e + \mathbf{D}^p. \quad (5)$$

Equations (1)–(5) are supplemented with the following constitutive relations:

$$\dot{\sigma}_{ij} + \sigma_{ik}W_{kj} - \sigma_{jk}W_{ik} = \frac{E(1-f)}{1+\nu}D_{ij}^e + \frac{E(1-f)\nu}{(1+\nu)(1-2\nu)}(D_{kk}^e - \hat{\alpha}\dot{\theta})\delta_{ij}, \quad (6)$$

$$\dot{e} = c\tau\ddot{\theta} + c\dot{\theta} + \frac{1}{\rho(1-f)}\sigma_{ij}D_{ij}^e, \quad (7)$$

$$T_{i\alpha} = J\sigma_{ij}(F^{-1})_{\alpha j}, \quad (8)$$

$$q_i = -\kappa\left(1 - \frac{3}{2}f\right)\theta_{,i}, \quad Q_\alpha = Jq_i(F^{-1})_{\alpha i}, \quad (9)$$

$$\phi \equiv \frac{\sigma_e^2}{\sigma_y^2} - 1 + 2f^*\beta_1 \cosh\left(\frac{\beta_2\bar{p}}{2\sigma_y}\right) - \beta_1^2(f^*)^2 = 0, \quad \sigma_e^2 = \frac{3}{2}\sigma'_{ij}\sigma'_{ij}, \quad i, j = 1, 2, 3, \quad (10)$$

$$D_{ij}^p = \dot{\lambda} \frac{\partial \phi}{\partial \sigma_{ij}} = \dot{\lambda} \left[ \frac{3\sigma'_{ij}}{\sigma_y^2} - \frac{f^*\beta_1\beta_2}{\sigma_y} \sinh\left(\frac{\beta_2\bar{p}}{2\sigma_y}\right) \delta_{ij} \right], \quad \sigma'_{ij} = \sigma_{ij} + p\delta_{ij}, \quad (11)$$

$$p = -(\sigma_{11} + \sigma_{22} + \sigma_{33})/3, \quad \bar{p} = pH(-p - 0), \quad (12)$$

$$\dot{\lambda} = \frac{(1-f)\sigma_y\dot{e}_e^p}{\sigma_{ij} \frac{\partial \phi}{\partial \sigma_{ij}}}, \quad (13)$$

$$\dot{f} = (1 - f)D_{ii}^p + \frac{f_2 \dot{\varepsilon}_e^p}{s_2 \sqrt{2\pi}} e^{-\frac{1}{2} \left( \frac{\varepsilon_e^p - \varepsilon_n}{s_2} \right)^2} H(-p - 0), \quad (14)$$

$$f^* = \begin{cases} f, & f \leq f_c, \\ f_c + \frac{f_u - f_c}{f_f - f_c} (f - f_c), & f > f_c, \end{cases} \quad (15)$$

$$\sigma_y = (A + B(\varepsilon_e^p)^n) \left( 1 + C \ln \left( \frac{\dot{\varepsilon}_e^p}{\dot{\varepsilon}_0^p} \right) \right) \left( 1 - \left( \frac{\theta - \theta_r}{\theta_m - \theta_r} \right)^m \right). \quad (16)$$

The left-hand side of Equation (6) equals the Jaumann derivative of the Cauchy stress tensor  $\sigma$ ,  $W_{ij} = (v_{i,j} - v_{j,i})/2$  is the spin tensor,  $E$  Young's modulus,  $\nu$  Poisson's ratio,  $\hat{\alpha}$  the coefficient of thermal expansion,  $\delta_{ij}$  the Kronecker delta,  $c$  the specific heat,  $\tau$  the thermal relaxation time,  $\kappa$  the thermal conductivity of the solid material, and  $\theta$  the present temperature of a material particle. Batra and Jaber (2001) found that the Jaumann and the Green-Naghdi stress rates in Equation (6) give virtually identical results for the initiation of a shear band and a brittle failure at points near the surface of a notch-tip in a prenotched plate. This is because elastic strain rates appearing in Equation (6) are very small as compared to the plastic strain rates at points near the notch-tip.  $\phi = 0$  describes the yield surface proposed by Gurson (1977) for a porous material,  $p$  is the hydrostatic pressure, and  $f^*$  the modified value of the porosity given by (15). Gurson's model is based on quasistatic analysis with the matrix material modeled as rigid perfectly plastic and obeying von Mises yield criterion. Wang and Jiang (1997) have considered inertia effects. Wang (1997) has analyzed transient deformations of a single spherical void in a solid spherical shell made of a power-law heat-conducting viscoplastic material. For a microporous material, Wang (1997) derived an approximate expression for the macro-stress potential through an upper bound approach. Constants  $\beta_1$  and  $\beta_2$ , introduced by Tvergaard (1981), provide a better fit of results computed from a FE analysis of the formation of adiabatic shear bands in a plate having an array of large cylindrical voids with test observations, and  $\lambda$  is the factor of proportionality defined by (13).  $\sigma_y$  is the current yield stress of the material whose dependence upon the effective plastic strain  $\varepsilon_e^p$ , the effective plastic strain rate  $\dot{\varepsilon}_e^p$  and the temperature  $\theta$  is described by the Johnson-Cook (1983) relation (16) in which  $A$ ,  $B$ ,  $C$ ,  $\dot{\varepsilon}_0^p$ , and  $m$ , are material parameters,  $\theta_r$  the room temperature and  $\theta_m$  the melting temperature of the material. Parameters  $B$  and  $n$  characterize the strain hardening of the material,  $C$  and  $\dot{\varepsilon}_0^p$  the strain-rate hardening and the last factor on the right-hand side of (16) its thermal softening. Equation (14) gives the evolution of the porosity; the first term on its right-hand side is derived by assuming that the matrix is incompressible and the elastic dilatation is negligible as compared to the plastic dilatation, and the second term is the strain based nucleation of voids introduced by Chu and Needleman (1980).  $f_2$ ,  $s_2$  and  $\varepsilon_n$  are material parameters; the rate of nucleation of voids is highest when  $\varepsilon_e^p$  equals  $\varepsilon_n$  and decays exponentially with the difference between  $\varepsilon_e^p$  and  $\varepsilon_n$ .  $H$  is the Heaviside step function. Thus the second term contributes to the evolution of the porosity at a point only when the hydrostatic pressure there is tensile. To account for the coalescence of neighboring voids, Tvergaard and Needleman (1984) enhanced the porosity, as given by Equation (15), after it reaches its critical value  $f_c$ . In Equation (15),  $f_f$  is the porosity at ductile fracture, and  $f_u = 1/\beta_1$  is the porosity when the yield surface has shrunk to a point. Equations (10) and (16) imply that the radius of the von Mises yield surface increases due to strain- and strain-rate hardening of the material

but decreases due to the softening induced by the temperature rise and the increase in porosity. The degradation of material properties due to the damage, taken here synonymous with the porosity, is indicated by Equations (6)–(10). The affine variation with the porosity of Young's modulus, the bulk modulus, the stress-temperature coefficient, and the heat capacity implies that the rule of mixture has been employed to find their effective values; the expression for the thermal conductivity in Equation (16) is due to Budiansky (1970). The interaction, if any, among neighboring voids has been tacitly ignored. Jiang and Batra (2002), among others, have considered this interaction. The shrinkage of the yield surface due to an increase in porosity described by Equation (10) can be appreciated by plotting the yield surface for two different values of  $f$  while keeping other variables fixed. Perzyna (1998) has given a different equation for the evolution of porosity.

Substitution from Equations (5), (7) and (9) into (4) gives the following hyperbolic heat equation:

$$\rho_0(1 - f_0)c(\tau\ddot{\theta} + \dot{\theta}) = \left( \kappa \left( 1 - \frac{3}{2}f \right) \theta_{,\alpha} \right)_{,\alpha} + J\sigma_{ij}D_{ij}^p. \quad (17)$$

The term  $J\sigma_{ij}D_{ij}^p$  equals the heating due to plastic working per unit reference volume; thus the Taylor-Quinney parameter has been set equal to 1. Except for a delay in the time of initiation of an adiabatic shear band other results remain unaffected by a lower value of the Taylor-Quinney factor. The form (17) of the hyperbolic heat equation is due to Cattaneo (1958) and Vernotte (1958). The thermal relaxation time  $\tau$  in it represents the time required to establish a steady state of heat conduction in an element suddenly exposed to a heat flux. According to Chester (1963)  $\tau$  equals  $3\kappa/\rho c V_0^2$  where  $V_0$  is the speed of an elastic wave. Thus for a typical steel,  $\tau = 1 \times 10^{-12}$ s, and  $\tau \simeq 25 \times 10^{-12}$ s for copper. Batra and Lear (2004), and Chen and Batra (2001) found that the finiteness of the thermal wave speed affects the time of initiation of an adiabatic shear band in a typical steel and the spacing between adjacent bands only when  $\tau \geq 10^{-6}$ s. Batra (1975) showed that a theory based on higher-order gradients of temperature gives a hyperbolic heat equation. However, in such a material, either thermal waves propagate at a finite speed or the linearized problem has a unique solution.

Initial and boundary conditions needed to complete the formulation of the problem are:

$$\begin{aligned} \mathbf{x}(\mathbf{X}, 0) &= \mathbf{X}, \quad \mathbf{v}(\mathbf{X}, 0) = \mathbf{0}, \quad \theta(\mathbf{X}, 0) = \theta_0, \quad \dot{\theta}(\mathbf{X}, 0) = 0, \quad \rho(\mathbf{X}, 0) = \rho_0, \\ \varepsilon_e^p(\mathbf{X}, 0) &= 0, \quad f(\mathbf{X}, 0) = f_0(\mathbf{X}), \\ T_{i\alpha}N_\alpha &= 0 \quad \text{on } \Gamma_t, \quad x_i = \bar{x}_i \quad \text{on } \Gamma_v, \quad Q_\alpha N_\alpha = 0 \quad \text{on } \partial\Omega. \end{aligned} \quad (18)$$

That is, the initial velocity and the initial rate of change of temperature are null, the initial temperature is uniform  $\theta_0$ , and the initial mass density is uniform  $\rho_0$ . The part  $\Gamma_t$  of the boundary  $\partial\Omega$  of the region  $\Omega$  occupied by the body in the reference configuration is traction free and positions of material particles on  $\Gamma_v$  are given as a function of time. Here  $\Gamma_t$  and  $\Gamma_v$  have been taken to be disjoint for simplicity. Boundary conditions involving the prescription of linearly independent components of  $T_{i\alpha}N_\alpha$  and  $x_i$  at the same point on  $\partial\Omega$  are admissible. The entire boundary  $\partial\Omega$ , including surfaces of the notch, is thermally insulated at all times.

On the edge surface  $\Gamma_v$  of the plate impacted by the cylindrical rod, we set

$$v_1(t)/v_0 = \begin{cases} 0.3t, & 0 \leq t \leq 2 \mu s, \\ (0.525 + 0.0375t), & 2 < t \leq 10 \mu s, \\ 0.9, & 10 < t \leq 30 \mu s, \\ 0.9 + (5.4 - 0.18t), & 30 < t \leq 35 \mu s, \end{cases} \quad (19)$$

$$\begin{aligned} T_{21} &= 0, \quad Q_1 = 0, & t \geq 0, \\ T_{11} &= 0, & t > 35 \mu s. \end{aligned}$$

Here,  $v_0$  is the speed of the projectile,  $v_1$  the velocity of the plate particles in the  $x_1$ -direction, the time  $t$  is reckoned from the instant of impact, and it has been assumed that the cylindrical rod contacts the plate edge for  $35 \mu s$ . However, during the last  $5 \mu s$  of contact, the velocity of plate particles gradually reduces to zero. Subsequently, the traction on the impacted surface is set equal to zero. The expression (19) for  $v_1$  is deduced by fitting straight lines to the data of Batra and Ravisankar (2000) who studied 3-dimensional deformations of the plate and the projectile. Equations (19)<sub>6</sub> and (19)<sub>7</sub> imply that the contact surface is smooth and thermally insulated. The stipulated boundary conditions simulate well experiments in which the prenotched plate rests on a table top. The effects of the frictional force between the plate and the table top and the heat conducted between the two have been neglected; the latter is very small because of the extremely short time elapsed prior to the development of failure in the plate.

Let  $\rho_0$ ,  $\dot{\epsilon}_R$ ,  $H$ ,  $\sigma_0$  and  $\theta_R$  be the reference mass density, the reference strain rate, the reference length, the reference stress and the reference temperature used to non-dimensionalize quantities. Then in terms of nondimensional variables indicated by the same symbols as before, Equations (2) and (17) become

$$\alpha_I(1 - f_0)\dot{v}_i = T_{i\alpha\alpha}, \quad i = 1, 2, \alpha = 1, 2, \quad (20)$$

$$\rho_0(1 - f_0)(\tau\ddot{\theta} + \dot{\theta}) = -\alpha_t \left( \left(1 - \frac{3}{2}f\right)\theta, \alpha \right)_{,\alpha} + J\sigma_{ij}D_{ij}^p, \quad i, j = 1, 2, \quad (21)$$

where

$$\alpha_I = \frac{\rho_0 \dot{\epsilon}_R^2 H^2}{\sigma_0}, \quad \alpha_t = \frac{\kappa}{\rho_0 c H^2 \dot{\epsilon}_R}, \quad \theta_R = \frac{\sigma_0}{\rho_0 c H^2 \dot{\epsilon}_R}. \quad (22)$$

$\alpha_I$  and  $\alpha_t$  are nondimensional measures of inertia and heat conduction effects respectively. Thus, for a given material, inertia effects are directly proportional to the square of the reference strain rate and the square of the reference length, and heat conduction effects are inversely proportional to the reference strain rate and the square of the reference length. This nondimensionalization of variables is the same as that employed by Batra and Kim (1992). A possible choice for  $H$  is the notch-tip radius  $r_0$ , and for  $\dot{\epsilon}_r$  is  $v_0/r_0$ .

Batra and Jin (1994) used the aforestated problem formulation to analyze the initiation of adiabatic shear bands in a microporous thermoviscoplastic body deformed in plane strain tension. They used a parabolic heat equation, and adaptively refined FE meshes of 3-node triangular elements. They showed that, for the steel studied, the softening of the material induced by porosity evolution was considerably more than that caused by heating of the material due to plastic working.

We note that Batra and Kim (1990), Batra and Jaber (2001) and Batra and Chen (2001a) have analyzed different aspects of shear banding with four different thermoviscoplastic relations, namely, the Johnson-Cook (1983), the Litonski-Batra (e.g., see, Batra, 1988), the Bodner-Partom (1975) and a power law. These relations were calibrated to give nearly the same effective stress vs. the effective strain curve during homogeneous deformations of the body. However, during inhomogeneous deformations, each one of the relations gave qualitatively similar but quantitatively different results. The decision to use the Johnson-Cook relation here is based on the availability of values of thermomechanical parameters for different materials.

### 3. Weak formulation of the problem

Equations (6), (8) and (3) imply that the balance of moment of momentum (3) is identically satisfied. The present mass density can be computed from Equation (1) if the deformation gradient and the current value of the porosity are known. Thus, the dependent variables to be solved for are  $\mathbf{x}$ ,  $f$  and  $\theta$  and the independent variables are  $\mathbf{X}$  and  $t$ . Equations (20) and (21) are second-order coupled non-linear hyperbolic partial differential equations for  $\mathbf{x}$  and  $\theta$ . These can not be written explicitly in terms of  $\mathbf{x}$  and  $\theta$  since  $\mathbf{T}$  is given by (8) and  $\sigma$  by (6) which involves  $\mathbf{D}^p$  and  $\theta$ . In order to solve the problem numerically by the FEM, we first derive its weak formulation.

Let  $\mathbf{w}(\mathbf{X})$  be a smooth function that vanishes on  $\Gamma_v$ . We take the inner product of Equation (20) with  $\mathbf{w}$ , integrate the resulting eqn. over the region  $\Omega$  occupied by the body in the reference configuration, and use the divergence theorem and the natural boundary condition (18)<sub>8</sub> on  $\Gamma_t$  to arrive at

$$\int_{\Omega} \alpha_I (1 - f_0) \dot{v}_i w_i d\Omega = - \int_{\Omega} w_{i,\alpha} T_{i\alpha} d\Omega + \int_{\Gamma_t} w_i \bar{t}_i d\Gamma. \quad (23)$$

Let  $\psi_1, \psi_2, \dots, \psi_n$  be FE basis functions defined on  $\Omega$ . We write

$$\begin{aligned} v_i &= \sum_{A=1}^{\text{nodes}} \psi_A(\mathbf{X}) \tilde{v}_{Ai}(t), \quad i = 1, 2, \\ w_i &= \sum_{A=1}^{\text{nodes}} \psi_A(\mathbf{X}) c_{Ai}, \quad i = 1, 2. \end{aligned} \quad (24)$$

Here  $\tilde{\mathbf{v}}$  is the vector of velocities of nodes, and  $c$ 's are constants. Substituting from (24) into (23) and exploiting the fact that the resulting eqn. must hold for all choices of  $c$ 's we get

$$\begin{aligned} \mathbf{M}\dot{\tilde{\mathbf{v}}} &= \mathbf{F}^{\text{ext}} - \mathbf{F}^{\text{int}}, \\ M_{AB} &= \int_{\Omega} \alpha_I (1 - f_0) \psi_A \psi_B d\Omega, \\ F_{Ai}^{\text{int}} &= \int_{\Omega} \psi_{A,\alpha} T_{i\alpha} d\Omega, \\ F_{Ai}^{\text{ext}} &= \int_{\Gamma_t} \psi_A \bar{t}_i d\Gamma, \end{aligned} \quad (25)$$

where  $\bar{t}_i$  is the traction vector prescribed on the boundary  $\Gamma_t$ . For our problem,  $\bar{t}_i = 0$ .

In order to derive a weak form of Equation (21) we first introduce an auxiliary variable defined by

$$\xi = \dot{\theta}, \quad (26)$$

and adopt the same procedure as that used to derive Equation (25)<sub>1</sub> with the following result:

$$\begin{aligned} \dot{\theta} &= \tilde{\xi}, \\ \tau \mathbf{H} \dot{\tilde{\xi}} + \mathbf{H} \tilde{\xi} &= \mathbf{F}^\theta + \bar{\mathbf{Q}}, \end{aligned} \quad (27)$$

where

$$\begin{aligned} H_{AB} &= \int_{\Omega} \rho_0 (1 - f_0) \psi_A \psi_B d\Omega, \\ F_A^\theta &= \int_{\Omega} \alpha_t \left( 1 - \frac{3}{2} f \right) \theta_{,\alpha} \psi_{A,\alpha} d\Omega, \\ Q_A &= \int_{\Omega} \psi_A J \text{tr}(\sigma \mathbf{D}^p) d\Omega. \end{aligned} \quad (28)$$

Note that the natural boundary condition of zero heat flux has been embedded in Equation (27)<sub>2</sub>.

We solve Equation (16) for  $\dot{\varepsilon}_e^p$  in terms of  $\sigma_y$ ,  $\varepsilon_e^p$  and  $\theta$  and derive its weak form in the same way as before except that the divergence theorem is not used. Recall that  $\dot{\varepsilon}_e^p > 0$  only when a material point is deforming plastically as signified by the satisfaction of Equation (10)<sub>1</sub>; otherwise  $\dot{\varepsilon}_e^p = 0$ . Weak forms of Equations (6), (14) and

$$\dot{\mathbf{x}} = \mathbf{v}(\mathbf{X}, t), \quad (29)$$

are also derived. We thus get coupled nonlinear ordinary differential equations

$$\dot{\mathbf{d}} = \mathbf{F}, \quad (30)$$

where  $\mathbf{d}$  is the vector of unknowns and  $\mathbf{F}$  is the force vector that depends upon time  $t$  and  $\mathbf{d}(t)$ . The twelve unknowns at a node are  $\{x_1, x_2, v_1, v_2, \sigma_{11}, \sigma_{22}, \sigma_{12}, \sigma_{33}, f, \theta, \xi, \varepsilon_e^p\}$ . For a 3-node triangular element, each one of these variables is a polynomial of degree 1 in the  $X_1$  and  $X_2$  coordinates of nodes. Recall that natural boundary conditions are embedded in (30). Equations (30) are modified to enforce essential boundary conditions (19) at nodes on the impact surface, and are then integrated by using the subroutine LSODE (Livermore Solver for Ordinary Differential Equations) with parameter MF in LSODE set equal to 10 and parameters  $ATOL = RTOL = 10^{-7}$ .  $ATOL$  and  $RTOL$  control the absolute and the relative tolerances in the computed solution.  $MF = 10$  implies that the subroutine uses the Adams-Moulton method of integrating ODEs. LSODE adaptively adjusts the size of the time step and the order of the method in order to compute the solution within the prescribed accuracy. The subroutine can be downloaded from the internet.

#### 4. Failure criteria

In order to determine the impact speed at which the failure mode changes from brittle to ductile or vice-versa, we need a criterion for the failure mode initiation. Ritchie et al. (1973) have proposed that the brittle failure initiates at a point when  $\sigma_p/\sigma_0 = 3.0$  over a certain length which is characteristic of the microstructure of the material and generally equals a grain diameter. Here  $\sigma_p$  is the maximum tensile principal stress at a point and  $\sigma_0$  the yield stress in a quasistatic simple tension test. Tensile experiments of Hendrickson et al. (1958) at nominal stress rates of about 1 to  $10^4 \text{ MPa s}^{-1}$  show that brittle failure occurs at  $\sigma_p/\sigma_0 = 2.34$  for a prenotched steel specimen with a yield stress of 705 MPa. This value of  $\sigma_p/\sigma_0$  was found to be essentially independent of the temperature and the rate of loading. In numerical simulations, Zhou et al. (1996b), Batra and Gummalla (2000); Batra and Ravisankar (2000), Batra and Jaber (2001), and Batra et al. (2003) presumed that the brittle failure initiates when  $\sigma_p/\sigma_0 = 3.0, 2.0, 2.0, 2.34$  and  $2.34$ , respectively. Here, we assume that the brittle failure initiates when  $\sigma_p/\sigma_0 = 2.0$ . Our goal is to analyze the effect crack opening and propagation has on the deformation fields; thus, the precise value of  $\sigma_p/\sigma_0$  at the instant of the brittle failure initiation is less critical.

Ductile failure is generally believed to occur due to the nucleation and coalescence of voids within an adiabatic shear band (ASB). However, previous analyses of the problem by Needleman and Tvergaard (2000), and Batra and Jaber (2001) have shown that the maximum value of the porosity reached is about 0.03 which is far from 0.25, the value for the initiation of a ductile failure (e.g., see, Curran et al., 1987). Accordingly, the ductile failure is assumed to initiate at a point when an ASB forms there.

Batra and Rattazzi (1997) studied the initiation and propagation of an ASB in a thick-walled steel tube and found that the choice of the ASB formation criterion will affect the predicted initiation time. They used four different criteria: (i) the effective plastic strain at a point equals 0.5 and the material point is deforming plastically, (ii) the effective plastic strain at a point equals 1.0 and the material point is deforming plastically, (iii) the effective stress has dropped to 90% of its peak value and the material point is deforming plastically, and (iv) the effective stress has dropped to 80% of its maximum value and the material point is deforming plastically. By studying numerically the initiation of an ASB in twelve materials deformed in simple shear, Batra and Kim (1992) proposed the ASB criterion like (iii) and (iv). Since the time of initiation of an ASB depends upon the criterion, the impact speed at which failure mode transition occurs will also depend upon this choice. Here we adopt criterion (i). Zhou et al. (1996b) estimated the quasistatic yield stress of their C-300 steel to be 2 GPa, and assumed that the ductile failure initiated at a point when the effective plastic strain there equalled 0.04. Also, the flow stress was assumed to decrease exponentially with the temperature rise. Their computations showed only ductile failure which is consistent with their experimental observations.

#### 5. Simulation of crack propagation

In order to simulate crack initiation and propagation, we assume that as soon as a failure criterion is met at a node, say  $N$ , an additional node  $N^*$ , coincident with  $N$  but not connected to it, is added to the FE mesh. The node  $N^*$  is connected to the node  $N^{**}$  that has the next highest value of  $\sigma_p$  for the propagation of the brittle failure and of  $\varepsilon_e^p$  for the propagation of the ductile failure. The elements are adjusted such that all nodes originally connected to

$N$  on one side of the newly formed crack are connected to  $N^*$  instead. Thus lines  $NN^{**}$  and  $N^*N^{**}$  overlap at the instant of the initiation of a fracture and each is an interelement boundary between two adjoining elements. Note that no new element is created; however, a node is added, the element connectivity is modified and the number of unknowns is increased. Subsequent deformations of the body will either move  $N$  and  $N^*$  apart or tend to push them together. In the former case, surface tractions and the normal component of the heat flux are assumed to be null on the crack surfaces. In the latter case, in order to prevent interpenetration of the material through the crack surfaces, small 2-node stiff-spring elements, weak in tension but stiff in compression, are added between nodes  $N$  and  $N^*$ . The constitutive relation for the stiff-spring is taken to be

$$F = kx_n, \quad (31)$$

where

$$k = \begin{cases} 0, & x_n/x_0 \geq 0, \\ E\ell \left[ 1 + (\eta E - 1) \left( \frac{x_n}{x_0} \right)^2 \right], & -1 \leq x_n/x_0 < 0, \\ \eta E\ell, & x_n/x_0 < -1. \end{cases} \quad (32)$$

Here  $F$  is the normal force between nodes  $N$  and  $N^*$ ,  $E$  Young's modulus of the matrix material,  $x_n$  the relative displacement between nodes  $N$  and  $N^*$  normal to the crack surface,  $\ell$  a characteristic length, and  $\eta$  is constant. Equations (31) and (32) imply that the normal force between nodes  $N$  and  $N^*$  equals zero when they are separate but tends to push them apart in case of interpenetration.

## 6. Computation and discussion of results

Results are computed for a 4340 steel plate and impact speeds of 20, 30, 50 and 60 m/s. Values of material parameters in the Johnson-Cook relation (16) and Equations (6), (7), (10), (14), (31) and (32) are:

$$\begin{aligned} \sigma_0 = A = 792.19 \text{ MPa}, B = 509.51 \text{ MPa}, C = 0.014, m = 1.03, n = 0.26, \theta_m = 1793 \text{ K}, \\ \hat{\alpha} = 10^{-6} / \text{K}, \kappa = 38 \text{ W/mK}, c = 477 \text{ J/kg K}, \rho = 7840 \text{ kg/m}^3, \nu = 0.27, \tau = 10^{-8} \text{ s}, \\ \beta_1 = 1.5, \beta_2 = 1.0, f_2 = 0.04, s_2 = 0.1, \theta_r = 273 \text{ K}, E = 210 \text{ GPa}, \\ \varepsilon_n = 10, f_c = 0.15, f_u = 2/3, f_f = 0.25, \\ \eta = 10, x_0 = 0.01 \text{ mm}, \ell = 1 \text{ mm}. \end{aligned} \quad (33)$$

Because of the symmetry of the plate geometry and the initial and boundary conditions, deformations of the plate will be symmetric about the  $X_1X_3$ -plane passing through the plate centroid. Thus deformations of the upper half of the plate are analyzed.

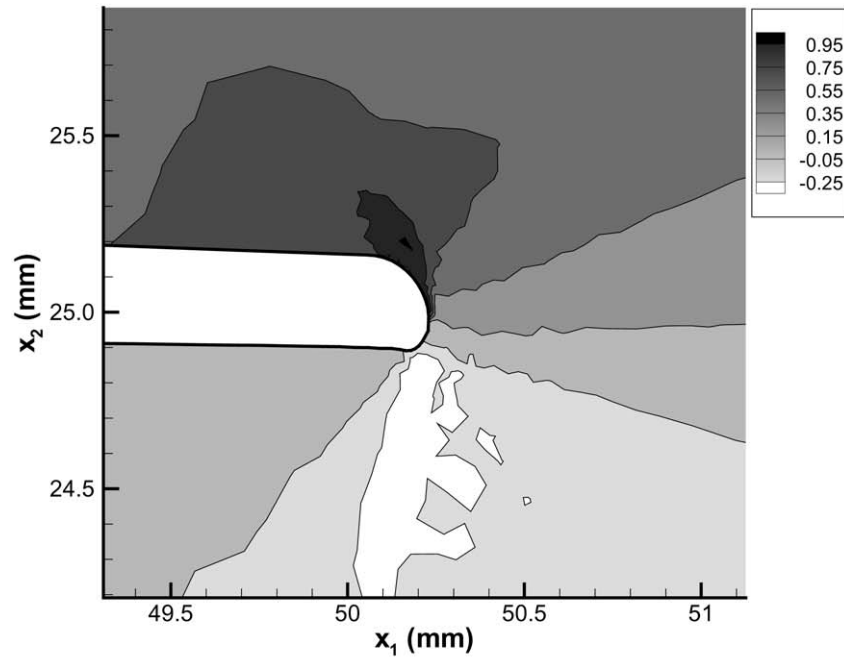
For values of material parameters listed in (33), the thermal wave speed equals 32 m/s which is two orders of magnitude less than the speed of an elastic wave. Thus the size of the time step in the numerical integration of the ODEs is governed by the speed of an elastic wave.

An unstructured mesh of 3,998 3-node triangular elements with 21 evenly spaced nodes around the notch-tip generated by using TECPLOT is employed. Fine elements are placed

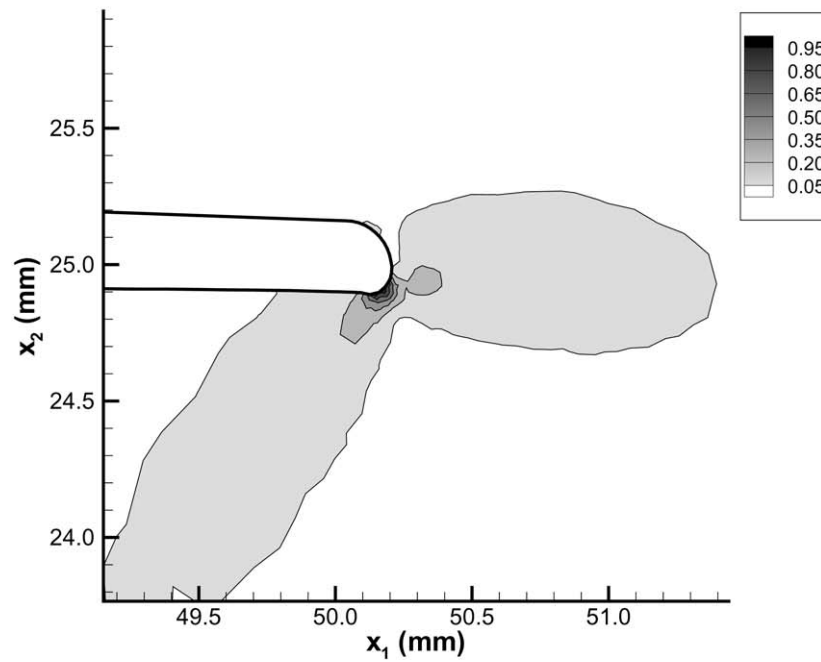
in the region around the notch-tip and the mesh gets coarser as one moves away from the notch-tip. The mesh is quite coarse in the top left portion of the plate because the material there is not deformed much. The computed results at different points on the notch-tip surface for the nondimensional maximum principal stress ( $\sigma_p/2\sigma_0$ ) and the effective plastic strain from this mesh were found to be very close to those from a finer mesh with 8,712 3-node triangular elements and 41 evenly spaced nodes around the notch-tip. Furthermore, each set of results essentially matched with that found in earlier studies of the problem (e.g., see, Batra and Jaber, 2001); these are not reported here. In order to prevent contact between points on the two surfaces of a notch during deformations of the prenotched plate, the surface of the notch that is away from the impacted edge is taken to be inclined rather than being horizontal; the same strategy was adopted by Batra and Nechitailo (1997), and Batra and Gummalla (2000). It should not affect deformations of the material directly ahead of the impacted surface and of material points on the notch-tip.

The impact of the plate by the rod causes a compressive longitudinal wave to travel into the plate towards the notch-tip. For values of  $E$ ,  $\nu$ , and  $\rho$  used for the plate material, analytical speed for the longitudinal wave equals 5.77 mm/ $\mu$ s. Because of the interaction among deformations of nodes as represented by nondiagonal mass and stiffness matrices, the computed wave speed is usually larger than the analytical value; the difference between the two speeds depends upon the FE mesh, and the method employed to integrate coupled ODEs (30). Upon arrival of the wave at the notch-tip, the material there is significantly deformed because deformations are essentially singular. The computed velocity field in the plate is similar to that plotted in Figure 4 of Batra and Gummalla's (2000) paper and is not shown here. Material particles adjacent to the lower traction free surface of the notch move to the right, i.e., in the direction of the applied velocity  $\mathbf{v}_0$ , and those close to the upper traction free surface of the notch are essentially stationary till the loading wave arrives at the notch-tip. The displacement in the direction of  $\mathbf{v}_0$  of particles on the lower surface of the notch stretches material lines on the curved surface of the notch, distorts the shape of the notch-tip, and induces a tensile hoop stress at points on the upper surface of the notch-tip. The maximum tensile principal stress occurs at a point inside the body near the notch surface at a point that in the reference configuration makes an angle of approximately  $70^\circ$  counterclockwise with the notch-axis. This point is hereafter referred to as point *B*. The effective plastic strain is maximum at a point on the lower notch-tip surface. This point is hereafter referred to as point *D*. Coordinates of points *B* and *D* in the reference configuration are (50.09 mm, 25.20 mm) and (50.08 mm, 24.87 mm), respectively. Lines joining *B* and *D* to the center of the circular notch-tip make angles of  $65.8^\circ$  counterclockwise and  $58.4^\circ$  clockwise with the axis of the notch. These are in general agreement with the observations of Kalthoff and Winkler (1987), and also of previous numerical investigations (e.g., see, Batra and Jaber, 2001).

For an impact speed of 50 m/s, Figure 2a depicts contours of the nondimensional maximum principal stress, ( $\sigma_p/2\sigma_0$ ), in a small region around the notch-tip immediately prior to the occurrence of the brittle failure ( $\sigma_p/2\sigma_0 = 1$ ). For an impact speed of 60 m/s, Figure 2b depicts contours of the effective plastic strain/the effective plastic strain at ductile failure ( $\varepsilon_e^p/\varepsilon_c$ ) in a small region around the notch-tip immediately prior to the onset of the ductile failure ( $\varepsilon_e^p/\varepsilon_c = 1$ ). It is clear from Figure 2 that brittle failure will initiate at a point close to the upper notch surface and ductile failure will initiate at a point on the lower notch surface. The shape of the plastically deformed zone indicates that deformations of the material near the notch-tip correspond to neither pure mode-I nor pure mode-II; however, they are mode-II dominant. At plate particles directly ahead of the notch-tip, we have plotted in Figure 2c

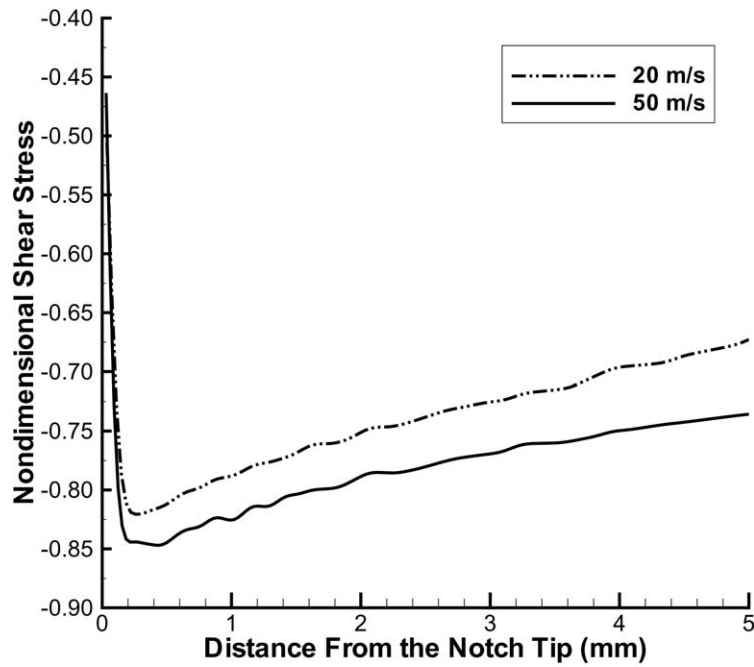


(a)



(b)

Figure 2. Contours of the (a) nondimensional maximum principal stress at  $t = 18 \mu\text{s}$  for  $v_0 = 50 \text{ m/s}$ , (b) contours of  $\varepsilon_e^p / \varepsilon_c$  at  $t = 15.1 \mu\text{s}$  for  $v_0 = 60 \text{ m/s}$ , and (c) the variation of the nondimensional shear stress at points directly ahead of the notch tip.

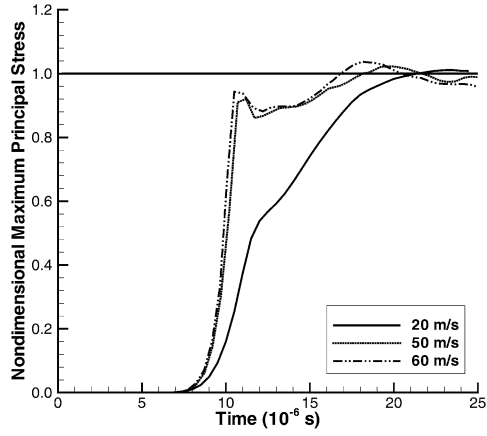


(c)

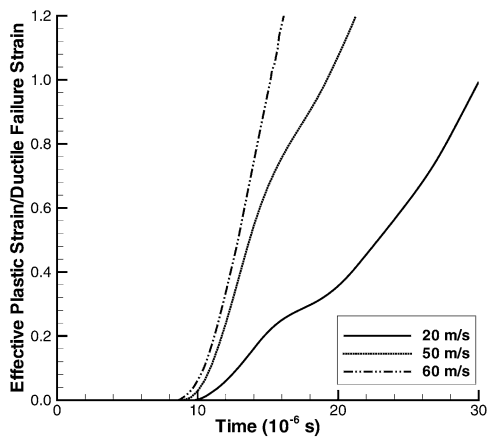
Figure 2. Continued.

the variation of the non-dimensional shear stress ( $\sigma_{12}/\sigma_0$ ) with the distance from the notch-tip. The traction free boundary condition on the notch surface requires that  $\sigma_{12} = 0$  at the notch-tip ( $r = 0$ ). For  $v_0 = 20$  and  $50$  m/s, the shear stress variation evinces a boundary layer in the sense that its magnitude increases rapidly, attains a maximum at  $r = 0.2$  mm, and then gradually decreases. The maximum value of  $|\sigma_{12}|$  is not that much affected by the impact speed. Ching and Batra (2001) were the first to identify this boundary layer; they analyzed static elastic deformations of the prenotched plate by the meshless local Petrov-Galerkin (MLPG) method. Batra and Ching (2002) studied elastodynamic deformations of a prenotched plate by the MLPG method and computed time histories of the stress intensity factors  $K_I$  and  $K_{II}$ . Results plotted in Figure 16 of their paper indicate that  $|\dot{K}_{II}|$  is higher than  $|\dot{K}_I|$  and for  $8 \leq t \leq 24 \mu\text{s}$ ,  $|K_{II}|$  continues to grow but  $|K_I|$  is nearly constant for  $t \geq 12 \mu\text{s}$ . Thus the mode-mixity parameter varies with time  $t$ , and results computed with modeling a notch by a sharp crack may not represent the true state of deformation near a notch-tip.

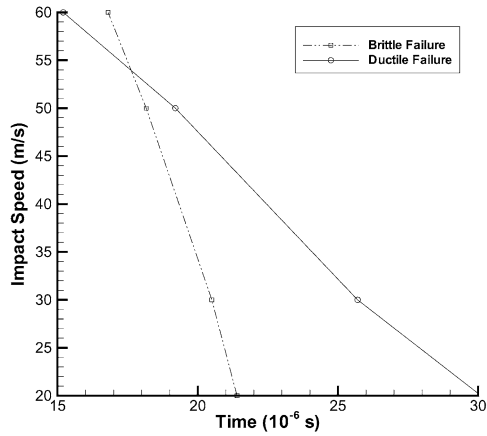
Time histories of evolution of the maximum principal tensile stress at point  $B$  and of the effective plastic strain at point  $D$  are exhibited in Figures 3a and 3b. These plots reveal the following: (i) the rate of rise of the effective plastic strain at point  $D$  and of the maximum principal stress at point  $B$  increase with an increase in the impact speed, (ii) the change in the peak value of the maximum principal stress induced at  $B$  is miniscule when the impact speed is increased from  $50$  m/s to  $60$  m/s; however, the increase in the effective plastic strain at  $D$  is considerable when the impact speed is increased from  $50$  m/s to  $60$  m/s, (iii) the brittle failure will likely initiate first at impact speeds of  $20$  and  $50$  m/s and the ductile failure at an impact speed of  $60$  m/s, (iv) the effective plastic strain rate increases with an increase in the



(a)



(b)



(c)

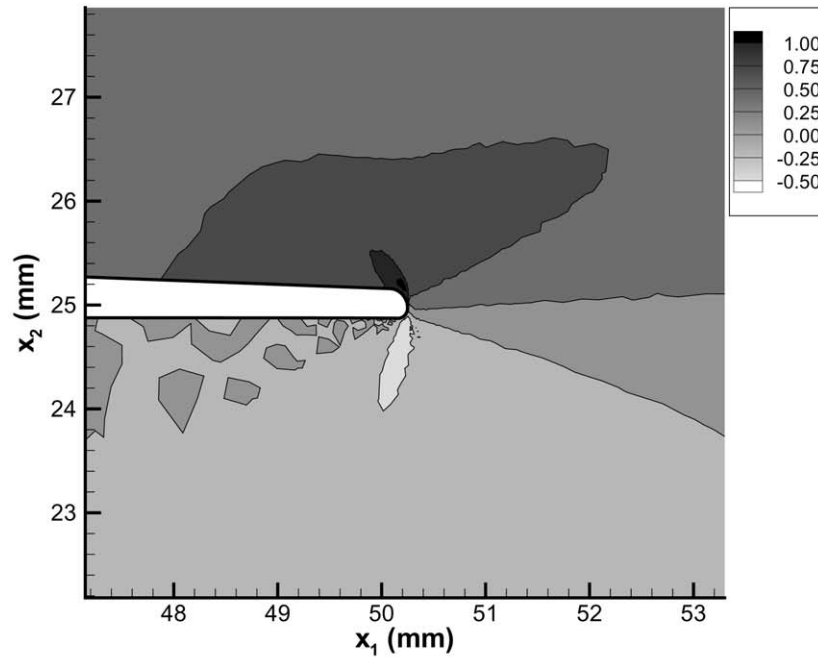
Figure 3. For  $v_0 = 20, 50,$  and  $60$  m/s, the time history of the evolution of (a) the nondimensional maximum principal stress at point  $B$  and (b)  $\varepsilon_e^P/\varepsilon_c$  at point  $D$ ; (c) The dependence of the time of initiation of the brittle and the ductile fracture upon the impact speed,  $v_0$ .

impact speed, and  $(v)$  for  $v_0 = 60$  m/s,  $\dot{\varepsilon}_e^p = 1.2 \times 10^5/s$ ,  $\dot{\sigma}_p \simeq 450$  MPa/s. The failure mode transition speed can be read from Figure 3c where plots of the time of initiation of the two failure modes against the impact speed are shown. Figure 3c indicates that the transition speed for this material and configuration is approximately 54 m/s. This failure mode transition speed differs noticeably from the 23 m/s computed by Batra and Jaber (2001) because of the differences in the values of the material parameters and the criteria employed for the initiation of the brittle and the ductile failures. Values of material parameters used by Batra and Jaber (2001) were such that the material exhibited considerably more thermal softening than the material studied here. Values of other material parameters in the two studies are also quite different. We note that times of initiation of the brittle and the ductile failures indicated in Figure 3c are without the opening of a crack. Once a crack starts from point  $B$ , the initiation of the ductile failure occurs at  $t = 52$  and  $22.2 \mu\text{s}$  for  $v_0 = 20$  and  $50$  m/s, respectively. Thus, the opening of a crack delays the initiation of the ductile failure, and the time lag is significant at low impact speeds. Similarly, for  $v_0 = 60$  m/s when a crack develops at point  $D$ , the initiation of the brittle failure at point  $B$  is postponed by  $1.7 \mu\text{s}$ .

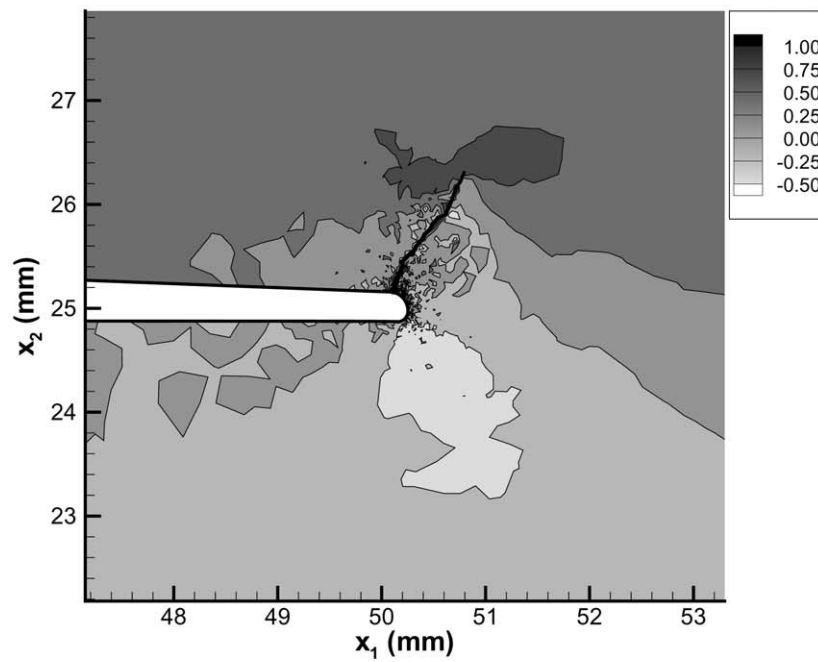
To simplify computations for the study of crack propagation, fracture is assumed to initiate either at a point on the notch surface or at a point on the nearly circular arc next to the notch surface. As shown in Figure 2, this method will accurately capture ductile fracture; however, it will not precisely capture the time of initiation of the brittle fracture. Using this assumption, the failure initiation times were  $24.5 \mu\text{s}$ ,  $18.5 \mu\text{s}$ , and  $15.2 \mu\text{s}$  for  $v_0 = 20$ ,  $50$ , and  $60$  m/s, respectively. The actual failure initiation times were found to be  $21.4 \mu\text{s}$ ,  $18.16 \mu\text{s}$ , and  $15.2 \mu\text{s}$ . For  $v_0 = 20$  m/s, Figures 4a and 4b exhibit contours of the maximum principal stress at  $t = 25 \mu\text{s}$  with and without modeling the opening of a crack at the point of initiation of the brittle failure. When stress fields in Figures 4a and 4b are compared with each other, it becomes apparent that the crack shifts the concentration of stresses from a point straight ahead of the starter notch-tip to that near the crack-tip. The sharp gradients in the effective stress formed adjacent to the traction free crack surfaces are due to oscillations associated with the formation of new surfaces and consequent emanation of elastic unloading surface (Rayleigh), longitudinal and transverse waves; the magnitude of oscillations diminishes with time. These transients could possibly have been diminished by gradually rather than immediately reducing the surface tractions to zero at points on the newly created surfaces. However, this was found to inhibit the growth of the crack.

Computed results can only be compared qualitatively with those of Kalthoff (1987) since he listed only the Rockwell hardness for the material of the plate. The time history of the crack length is given in Figure 5a for  $v_0 = 20$  and  $50$  m/s. For both cases, the crack grows affinely in time with a crack propagation speed of  $1.6$  km/s or  $28\%$  of the longitudinal wave speed for this material.

For both impact speeds, the crack propagated along a path that made an angle of approximately  $60^\circ$  counterclockwise with the axis of the notch. In Kalthoff's (1987) and Kalthoff and Winkler's (1987) experiments, the angle between the crack path and the notch axis equalled  $70^\circ$ . In a PC prenotched plate, Ravi-Chandar et al. (2000) observed that the maximum crack speed equalled about one-half of the Rayleigh wave speed. The crack in the PC plate initiated after waves had been reflected from the boundaries several times and the crack-tip was found to be under mixed-mode loading. As mentioned earlier Zhou et al. (1996a) did not observe brittle failure in their similar experiments on steel plates. The deformed shape of the plate after complete perforation ( $t = 80 \mu\text{s}$ ) for  $v_0 = 50$  m/s is shown in Figure 5b.

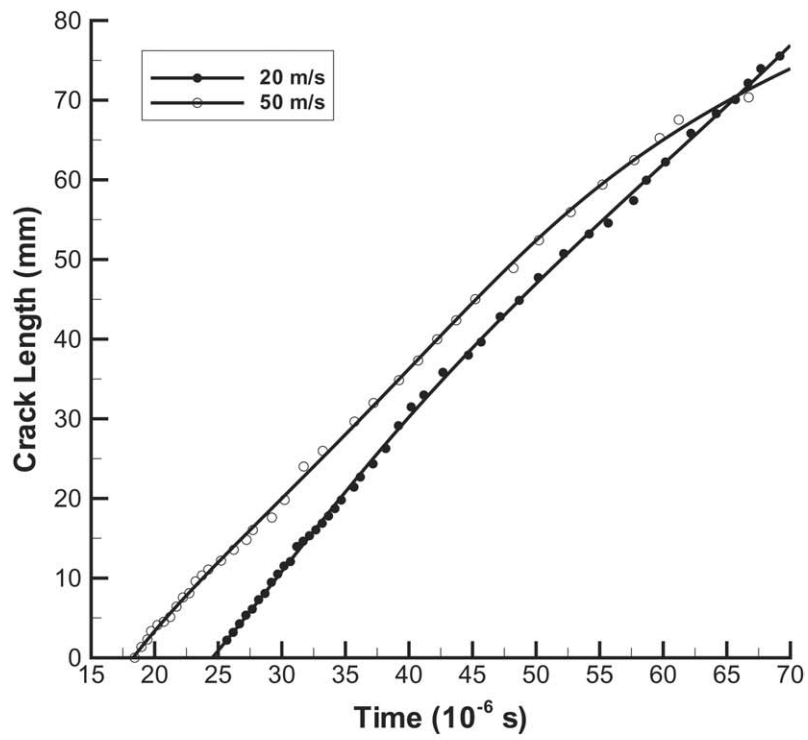


(a)

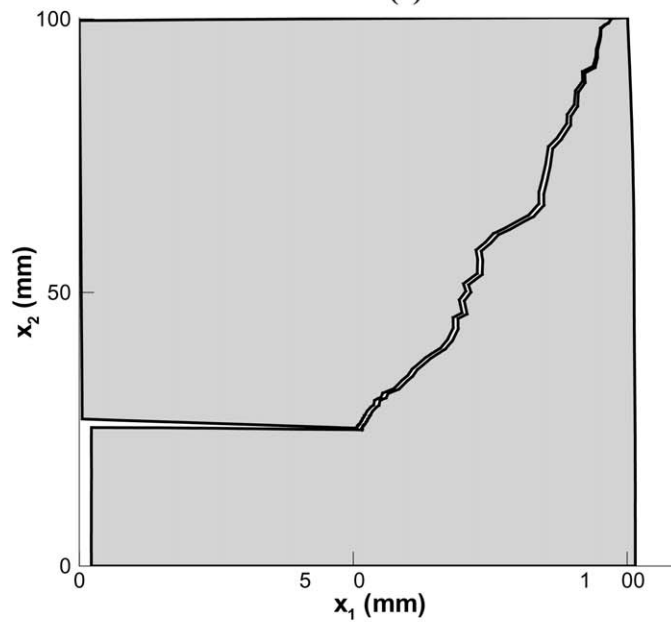


(b)

Figure 4. For  $v_0 = 20$  m/s, contours of the nondimensional maximum principal stress around the notch tip at  $t = 20 \mu\text{s}$  (a) without, and (b) with the opening of a crack at the point where brittle failure initiates.

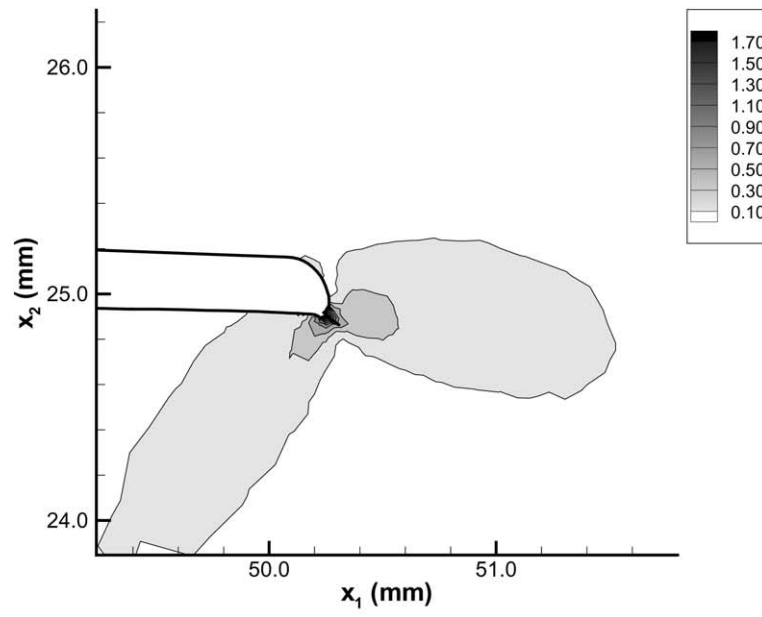


(a)

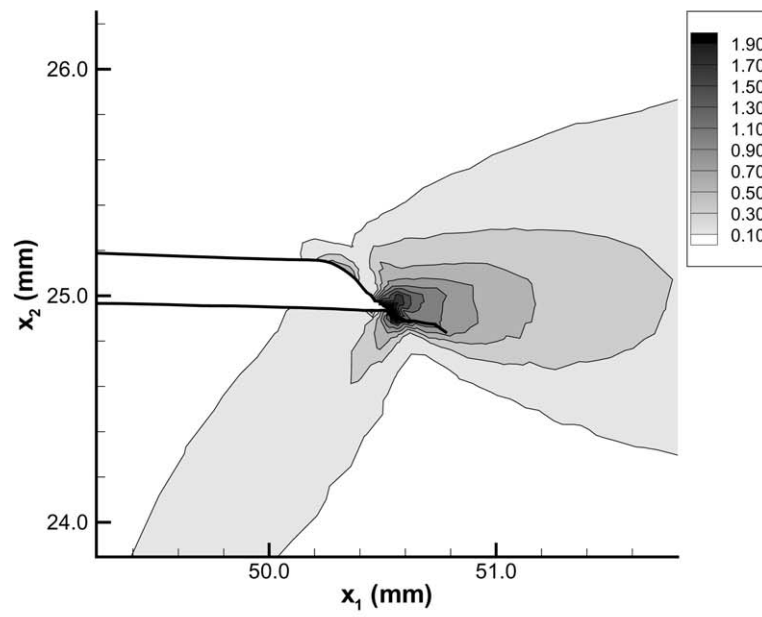


(b)

Figure 5. (a) The time history of the crack length for brittle failure for  $v_0 = 20$  m/s and  $v_0 = 50$  m/s and (b) the deformed shape of the plate at  $t = 100 \mu\text{s}$  for  $v_0 = 50$  m/s.



(a)



(b)

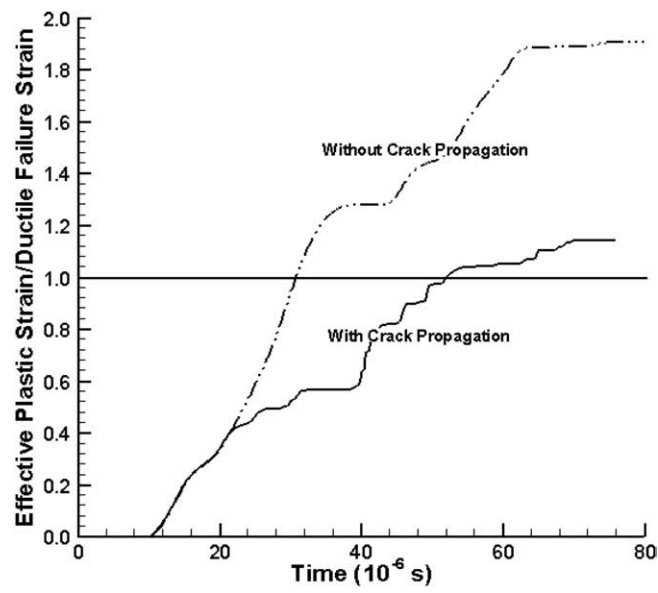
Figure 6. For  $v_0 = 60$  m/s, contours of  $\varepsilon_e^p/\varepsilon_c$  in a small region around the notch tip at (a)  $t = 21.5 \mu\text{s}$ , and (b)  $t = 33.5 \mu\text{s}$ .

For  $v_0 = 60$  m/s, the ductile failure preceded the brittle failure and initiated from point  $D$  on the notch surface. The ductile failure propagated along a line that in the present configuration makes an angle of  $15^\circ$  clockwise with the notch axis. We have plotted in Figures 6a and 6b, contours of the effective plastic strain immediately after the initiation of a crack due to the ductile failure, and at a later time. A comparison of results plotted in Figures 2b and 6a reveals that the presence of a crack due to the ductile failure does not have a significant effect on the general distribution of the effective plastic strain in a small region surrounding the lower portion of the notch-tip. However, at points close to the crack surface, the effective plastic strain is considerably higher than that at other points. In the deformed configuration depicted in Figure 6b, a leaflet like opening has formed in the intensely deformed region surrounding the lower surface of the notch-tip; a similar deformation pattern was computed by Batra and Gummalla (2000) who used DYNA2D, a mesh comprised of 4-node quadrilateral elements and neglected the effects of heat conduction and porosity. As the crack due to ductile failure propagates, the leaflet is incorporated into the crack surface.

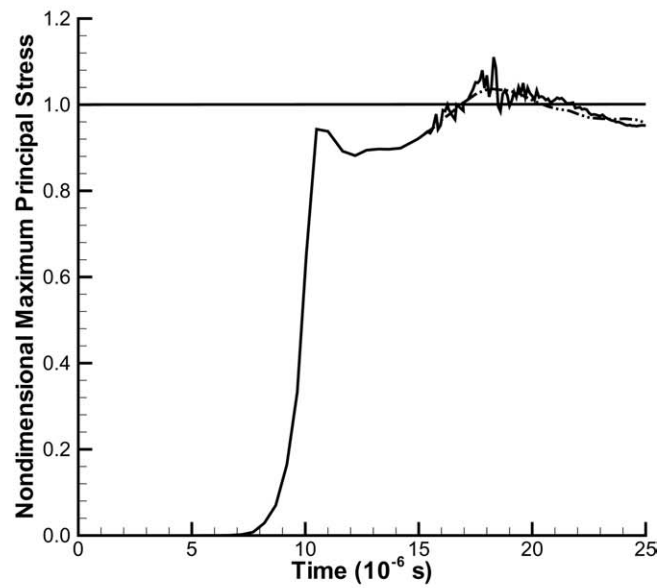
For  $v_0 = 20$  m/s, Figure 7a depicts the time history of the evolution of the effective plastic strain at point  $D$  both with and without the opening of a crack from point  $B$  where the brittle failure first occurs. It is clear that the opening of the crack at point  $B$  significantly influences the effective plastic strain developed at point  $D$ . However, as should be apparent from the results plotted in Figure 7b, the evolution of the principal stress at point  $B$  is not influenced by the opening of a crack at point  $D$  because the principal stress at point  $B$  has fully developed before a crack ensues from point  $D$ .

Contours of the temperature rise in the vicinity of the crack plotted in Figures 8a and 8b reveal that the maximum temperature rise near the crack surface increases from about 475 K to 775 K which equal approximately 25% and 45% of the melting temperature of the material. The maximum temperature occurs at a point on the crack surface that is behind the crack tip. The temperature rise at a point can be estimated by assuming that deformations are locally adiabatic and the material perfectly plastic. For an effective plastic strain of 1.9, and material parameters listed in (33), the approximate temperature rise equals  $(1.9)(792 \times 10^6)/(7840 \times 477)$  or 402 K. This value will increase when effects of strain- and strain-rate hardening are considered. The analysis was halted at  $t = 34 \mu\text{s}$  due to the excessive distortion of the mesh in the vicinity of the leaflet region. The crack length of 0.36 mm at this instant indicates that the ductile failure has not propagated much into the plate. A possibility is to adaptively refine the mesh within the severely deformed region and transfer from the previous mesh the state of deformation at nodes of the new mesh; however, this was not pursued because it smears out the deformation fields.

As mentioned at the beginning of Section 6, results computed with two unstructured meshes of 3,998 and 8,712 elements were found to be very close to each other. Nevertheless, numerical values of failure initiation times and crack propagation speed depend upon the FE mesh employed. One way to obtain mesh-independent results is to use a strain-rate gradient-dependent theory, e.g. see Batra (1987), and Batra and Hwang (1994). Such theories involve a material characteristic length and third-order spatial gradients of displacements in the problem formulation thereby necessitating the use of either Hermitian basis functions or auxiliary variables. At present, to our knowledge, there are no good ways of estimating the material characteristics length. Furthermore, these theories may either not give a finite speed of elastic waves or a unique solution of the linear elastic problem.

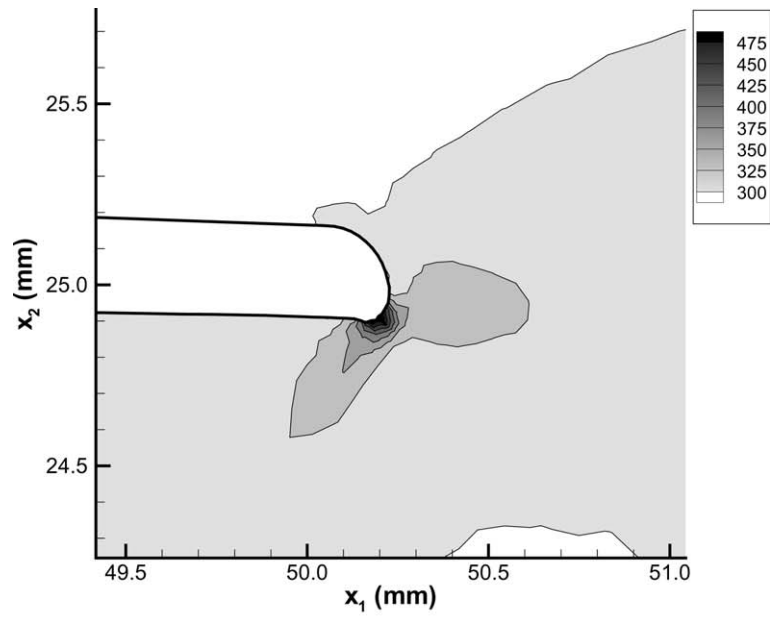


(a)

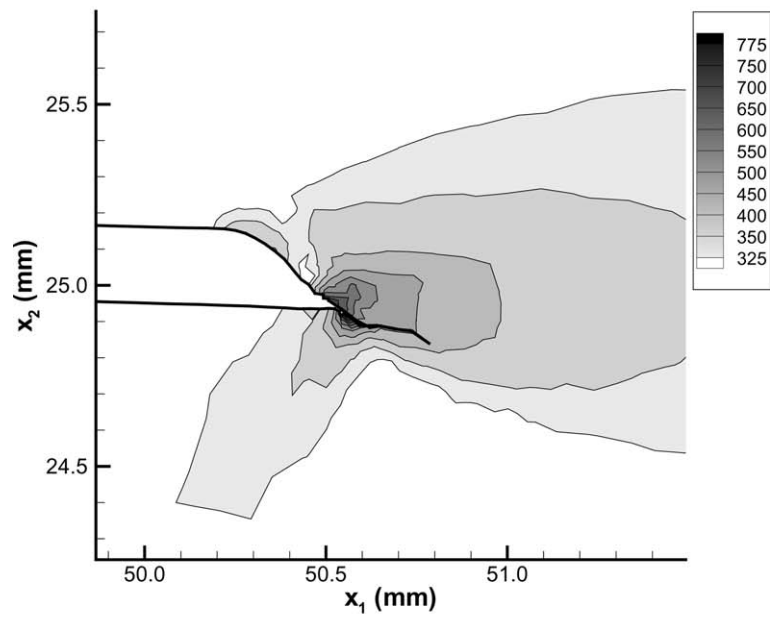


(b)

Figure 7. (a) The time history of  $\varepsilon_e^p/\varepsilon_c$  at point *D* both with and without the opening of a crack at point *B*, and (b) the time history of the nondimensional maximum principal stress at point *B* both with (solid line) and without (dotted line) the opening of a crack at point *D*. The two curves in (b) are nearly coincident.



(a)



(b)

Figure 8. For  $v_0 = 60$  m/s, contours of the temperature rise (K) in a small region around the notch tip at (a)  $t = 17.1 \mu\text{s}$ , (b)  $t = 33.7 \mu\text{s}$ .

## **7. Conclusions**

We have analyzed transient coupled thermomechanical deformations of a prenotched 4340 steel plate whose edge between the two parallel notches is impacted by a cylindrical projectile of diameter equal to the distance between the notches. The novel feature of the work is the simulation of the initiation and propagation of cracks due to brittle and ductile failures. It has been found that the brittle failure initiates first at low impact speeds and the ductile failure occurs first at high impact speeds and that for this configuration and material the failure mode transition occurs at an impact speed of approximately 54 m/s. The computed crack propagation speed of 1.6 km/s equals about 28% of the longitudinal wave speed of this material. The crack due to the brittle failure propagates all the way through the plate and splits it into two pieces. The opening of a crack at the point where brittle failure initiates delays the time of initiation of the ductile failure or an adiabatic shear band. However, for the ductile failure the propagation of only a small crack could be simulated due to excessive distortion of the mesh in the intensely deformed region. The opening of a crack at the point of initiation of the ductile failure does not influence the time of initiation of the brittle failure. The temperature rise in the vicinity of this small crack equalled approximately 45% of the melting temperature of the material. The initiation and propagation of a crack due to brittle failure noticeably influences the growth of the effective plastic strain at a point on the notch surface.

## **Acknowledgements**

This work was partially supported by the NSF grant CMS0002849, the ONR grant N00014-98-1-0300, the ARO grant DAAD19-01-1-0657, and the AFOSR MURI to Georgia Tech with a subcontract to Virginia Polytechnic Institute and State University. Opinions expressed in the paper are those of the authors and not of funding agencies.

## **References**

- Batra, R.C. (1975). On heat conduction and wave propagation in non-simple rigid solids. *Letters in Applied and Engineering Science* **3**, 97–107.
- Batra, R.C. (1987). The initiation and growth of, and the interaction among adiabatic shear bands in simple and dipolar materials. *International Journal of Plasticity* **3**, 75–89.
- Batra, R.C. and Hwang J. (1994). Dynamic shear band development in dipolar thermoviscoplastic materials. *Computational Mechanics* **12**, 354–369.
- Batra, R.C. and Jin, X.S. (1994). Analysis of dynamic shear bands in porous thermally softening viscoplastic materials. *Archives of Mechanics* **46**, 13–36.
- Batra, R.C. and Kim, C.H. (1992). Analysis of shear bands in twelve materials. *International Journal of Plasticity* **8**, 425–452.
- Batra, R.C. and Nechitailo N.V. (1997). Analysis of failure modes in impulsively loaded pre-notched plates. *International Journal of Plasticity* **13**, 291–308.
- Batra, R.C. and Gummalla, R.R. (2000). Effect of material and geometric parameters on deformations near the notch-tip of a dynamically loaded prenotched plate. *International Journal of Fracture* **101**, 99–140.
- Batra, R.C. and Ravisankar, M.V.S. (2000). Three-dimensional numerical simulation of the Kalthoff experiment. *International Journal of Fracture* **105**, 161–186.
- Batra, R.C. and Jaber, N.A. (2001). Failure mode transition in an impact loaded pre-notched plate with four thermoviscoplastic relations. *International Journal of Fracture* **110**, 47–71.
- Batra, R.C., Jaber, N.A. and Malsbury, M.E. (2003). Analysis of failure modes in an impact loaded thermoviscoplastic prenotched plate. *International Journal of Plasticity* **19**, 139–196.

- Batra, R.C. and Chen L. (2001). Effect of viscoplastic relations on the instability strain, shear band initiation strain, the strain corresponding to the maximum shear band spacing, and the band width in a thermoviscoplastic material. *International Journal of Plasticity* **17**, 1465–1489.
- Batra, R.C. and Chen, L. (2001). Instability analysis and shear band spacing in gradient-dependent thermoviscoplastic materials with finite speeds of thermal waves. *Archives of Mechanics* **53**, 167–192.
- Batra, R.C. and Ching, H.-K. (2002). Analysis of elastodynamic deformations near a crack-notch tip by the meshless local Petrov–Galerkin (MLPG) method. *Computer Modeling in Engineering and Sciences* **3**, 717–730.
- Batra, R.C. and Kim, K.H. (1990). Effect of viscoplastic flow rules on the initiation and growth of shear bands at high strain rates. *Journal of the Mechanics and Physics of Solids* **38**, 859–874.
- Batra, R.C. and Rattazzi, D. (1997). Adiabatic shear banding in a thick-walled steel tube. *Computed Mechanics* **20**, 412–426.
- Batra, R.C. and Lear, M.H. Adiabatic Shear Banding in Plane Strain Tensile Deformations of Thermoviscoplastic Materials with Finite Thermal Wave Speed, *submitted for publication*.
- Cattaneo, C. (1958). A form of heat equation which eliminates the paradox of instantaneous propagation. *CR Acad. Sci.* **247**, 431–433.
- Chester, M. (1963). Second sound in solids. *Phys. Rev.* **131**, 2103–2105.
- Ching, H.-K. and Batra, R.C. (2001). Determination of crack tip fields in linear elastostatics by the meshless local Petrov-Galerkin (MLPG) Method. *Computer Modeling in Engineering and Sciences* **2**, 273–289.
- Chu, C. and Needleman A. (1980). Void nucleation effects in biaxially stretched sheets. *Journal of Engineering Materials and Technology* **102**.
- Curran, D.R., Seaman, L. and Shockey, D.A. (1987). Dynamic failure of solids. *Physics Reports* **147**, 253–388.
- Gurson, A. L. (1977). Continuum theory of ductile rupture by void nucleation and growth: Part I. *Journal of Engineering Materials and Technology* **99**, 2–15.
- Hendrickson, J.A., Wood, D.S. and Clark, D.C. (1958). The initiation of brittle fracture in mild steel. *Journal of the Mechanics and Physics of Solids* **50**, 656–681.
- Jiang, B. and Batra, R.C. (2002). Effective properties of a piezocomposite containing shape memory alloy and inert inclusions. *Continuum Mech. Thermodynamics* **14**, 87–111.
- Johnson, G.R. and Cook, W.H. (1983). A constitutive model and data for metals subjected to large strains, high strain-rates, and high temperatures. *Proc. 7th International Symp. on Ballistics*, The Hague, The Netherlands, 541–548.
- Kalthoff, J.F. (1987). Shadow optical analysis of dynamic shear failure, SPIE, photomechanics and speckle. *Metrology* **814**, 531–538.
- Kalthoff, J.F. (2000). Modes of dynamic shear failure in solids. *International Journal of Fracture* **101**, 1–31.
- Kalthoff, J.F. and Winkler, S. (1987). Failure mode transition at high rates of shear loading. *Impact Loading and Dynamic Behavior of Materials* **1**, 185–195.
- Needleman A. (1987). A continuum model for void nucleation by inclusion debonding. *Journal of Applied Mechanics* **54**, 525–531.
- Needleman, A. and Tvergaard, V. (1995). Analysis of a brittle-ductile transition under dynamic shear loading. *International Journal of Solids and Structures* **32**, 2571–2590.
- Needleman, A. and Tvergaard, V. (2000). Numerical modeling of the ductile-brittle transition. *International Journal of Fracture* **101**, 73–97.
- Perzyna, P. (1998). Constitutive Modeling of Dissipative Solids for Localization and Fracture. In: *Localization and Fracture Phenomenon in Inelastic Solids*, (edited by P. Perzyna). pp. 99–242, Springer, Berlin.
- Ravi-chandar, K., Lu, J., Yang, B. and Zhu, Z. (2000). Failure mode transitions in polymers under high strain rate loading. *International Journal of Fracture* **101**, 33–72.
- Ritchie, R.O., Knott, J.F. and Rice, J.R. (1973). On the relationship between critical tensile stress and fracture toughness in mild steel. *Journal of the Mechanics and Physics of Solids* **21**, 395–410.
- Rousselier, G. (1987). Ductile fracture models and their potential in local approach to fracture. *Nuclear Engineering and Design* **105**, 97–111.
- Wang, Z.P. and Jiang, Q. (1997). A yield criterion for porous ductile media at high strain rate. *Journal of Applied Mechanics* **64**, 503–509.
- Wang, Z.P. (1997). Void-containing nonlinear materials subjected to high-rate loading. *Journal of Applied Physics* **81**, 7213–7227.

- Zhou, M., Ravichandran, G. and Rosakis, A. (1996a). Dynamically propagating shear bands in impact-loaded prenotched plates-I. *Journal of the Mechanics and Physics of Solids* **44**, 981–1006.
- Zhou, M., Ravichandran, G. and Rosakis A. (1996b). Dynamically propagating shear bands in impact-loaded prenotched plates-II. *Journal of the Mechanics and Physics of Solids* **44**, 1007–1032.